



Article

Modeling and Simulations of the Sulfur Infiltration in Activated Carbon Fabrics during Composite Cathode Fabrication for Lithium-Sulfur Batteries

Kyriakos Lasetta, Joseph Paul Baboo and Constantina Lekakou *

Department of Mechanical Engineering Sciences, University of Surrey, Guildford, Surrey GU2 7XH, UK; kl00602@surrey.ac.uk (K.L.); j.baboo@surrey.ac.uk (J.P.B.)

* Correspondence: c.lekakou@surrey.ac.uk

Abstract: During the manufacture of a composite cathode for lithium-sulfur (Li-S) batteries it is important to realize homogeneous infiltration of a specified amount of sulfur, targeted to be at least 5 mg cm^{-2} to achieve good battery performance in terms of high energy density. A model of the sulfur infiltration is presented in this study, taking into account the pore size distribution of the porous cathode host, phase transitions in sulfur, and formation of different sulfur allotropes, depending on pore size, formation energy and available thermal energy. Simulations of sulfur infiltration into an activated carbon fabric at a hot-plate temperature of $175 \text{ }^\circ\text{C}$ for two hours predicted a composite cathode with 41 wt% sulfur (8.3 mg cm^{-2}), in excellent agreement with the experiment. The pore size distribution of the porous carbon host proved critical for both the extent and form of retained sulfur, where pores below 0.4 nm could not accommodate any sulfur, pores between 0.4 and 0.7 nm retained S_4 and S_6 allotropes, and pores between 0.7 and 1.5 nm contained S_8 .

Keywords: composite cathode; sulfur infiltration; porous carbon host; modeling; computer simulations; sulfur allotropes



Citation: Lasetta, K.; Baboo, J.P.; Lekakou, C. Modeling and Simulations of the Sulfur Infiltration in Activated Carbon Fabrics during Composite Cathode Fabrication for Lithium-Sulfur Batteries. *J. Compos. Sci.* **2021**, *5*, 65. <https://doi.org/10.3390/jcs5030065>

Academic Editor: Francesco Tornabene

Received: 19 January 2021
Accepted: 20 February 2021
Published: 25 February 2021

Publisher's Note: MDPI stays neutral with regard to jurisdictional claims in published maps and institutional affiliations.



Copyright: © 2021 by the authors. Licensee MDPI, Basel, Switzerland. This article is an open access article distributed under the terms and conditions of the Creative Commons Attribution (CC BY) license (<https://creativecommons.org/licenses/by/4.0/>).

1. Introduction

Lithium-sulfur (Li-S) batteries are one of the latest generation lithium batteries, pursued due to their high theoretical energy density, 2510 Wh kg^{-1} [1], compared to an expected maximum of 250 Wh kg^{-1} for conventional Li-ion batteries [2–4]. Li-S batteries typically comprise a lithium anode and a composite sulfur cathode, consisting of sulfur as the active cathode material and a porous host, which provides electronic conductivity and structural integrity. Such hosts include activated carbon fabrics (ACF) [5], hollow nanofibers [6], hierarchically porous carbon coatings [7–10], graphene, and graphene oxide [11,12], where oxygen groups and functional, transition metal oxide groups [9,10] trap sulfur and polysulfides and thus reduce the “shuttling” effect during battery operation, and highly conductive materials such as carbon black and multiwall carbon nanotubes [13,14]. Furthermore, the porous carbon cathode host contributes a supercapacitor element [12,14–23], hence, increasing the power density of the Li-S battery. In this manner, a Li-S battery with such composite cathode is a hybridized battery/Li-ion capacitor [24], combining the high energy density of the Li-S battery and the high power density of the Li-ion capacitor (consisting of the lithium anode and porous carbon cathode), similarly to composite supercapacitors [25,26] but with much higher energy density, as the theoretical capacity of a Li-S battery reaches 1670 Ah g_s^{-1} (where g_s^{-1} denotes per gram of sulfur). A Li-S battery with a composite cathode can be easily recycled by disassembly [27] and liquid processing, dissolution of binder and sulfur [28,29], dielectrophoresis [30], and filtration techniques.

In order for the Li-S battery to achieve the expected high capacity and energy density, the amount of sulfur needs to be maximized in the composite cathode, recently specified above 5 mg cm^{-2} of cathode [31], with at least 70 wt% sulfur in the composite cathode

to minimize the weight of the redox-passive carbon host [1,6,7,11,31]. The infiltration stage is critical for the homogeneous sulfur impregnation through all host material and all pore sizes, while the porous host should have the required pore volume and pore size distribution to accommodate the specified amount and proportion of sulfur. There are different sulfur infiltration techniques in the porous cathode host [32]. Melt infiltration is the most common technique [5,6,8], where sulfur powder is placed on top of a fabric or other type of scaffold host or mixed with the carbon powder and heated above its melting point, where the lowest viscosity of sulfur is at 155 °C (20 mPa s), quickly rising to 54 Pa s at 165 °C and further as it polymerizes, reaching a maximum of 940 Pa s at 190 °C and falling thereafter to 60 Pa s at 280 °C [33]. Solution infiltration is another technique [12], rarely used because there are few good solvents for sulfur, all highly toxic, and there is the problem of solvent removal, usually by solvent evaporation, which would also lead to sulfur sublimation [12] that can easily take place even at relatively low temperatures between 25 and 50 °C [34]. Vapor infiltration [35] results in impregnation of smaller pores and shorter required duration of the infiltration process [35], where isothermal vapor infiltration at 135, 155, and 175 °C took place in 50, 30, and 7 min, respectively [35]. Although it can be seen that there is an overlap between the temperatures of the melt [5,13,32,33] and vapor processing [35], no investigations have been carried out, experimentally or theoretically, to resolve the proportion of melt and vapor contribution in the infiltration process at the usual infiltration temperatures in the range of 120–155 °C [5,13,32,33].

An additional question is which pore sizes may be able to accommodate sulfur and in which allotrope form, given that solid sulfur is typically encountered as octasulfur, S₈, but can also exist in other allotrope forms [36]. Activated porous carbons and graphene or graphene oxide have pore size distributions [5,9,10,24,25] including slit pores from 0.3 nm, representing interlayer spacing in graphite, 0.63 nm, and other pore sizes thereafter. While melt, solution, or vapor infiltration dynamics might resemble flow through porous media and could be modelled by Darcy's law [37], for example, there is the question of which pore sizes can accommodate which sulfur allotropes. No theoretical, modeling, or computational study has been carried out of the sulfur infiltration of the porous carbon cathode host.

We present, for the first time, a novel model of sulfur infiltration in parallel porous paths of different pore sizes from the pore size distribution of the porous cathode host with simultaneous heat transfer. In this model, we considered both sulfur sublimation and evaporation, as well as melting, of course, and formation of different sulfur allotropes depending on the pore size compared to the sulfur allotrope molecule size and also on the available thermal energy compared to the required sulfur allotrope formation energy. Computer simulations were carried out to predict sulfur retention and distribution for different sulfur allotropes in different pore sizes and across the cathode thickness. The predictions were compared with data of sulfur retention from an experimental study with an activated carbon fabric (ACF) host.

2. Materials and Experimental Methods

The cathode host was ACF Kynol[®] ACC-507-15 (Kynol Europe GmbH (Hamburg, Germany): areal density of 12 mg cm⁻² and specific surface area BET = 1461 m² g⁻¹), presented in Figure 1a,b, with a discretized pore size distribution (PSD) (Figure 1c) derived from data of nitrogen adsorption experiments [24]. The PSD started at 0.3 nm and exhibited peaks at 0.69 nm and 1.31 nm, which were in the micropore range. Micropores were expected to be of slit shape in phenolic-derived ACFs, as was the Kynol[®] fabric [24,38]. Figure 1b displays that macro- and mesopores of approximately circular cross section were also present and, during sulfur infiltration or battery operation, provided the transport channels for the transported species, sulfur, or ions [24], respectively, to reach the large proportion of micropores that dominated the PSD of the ACF. Sulfur powder (Sigma Aldrich, Gillingham, UK) was used as the active cathode material, via an infiltration stage into the porous ACF host.

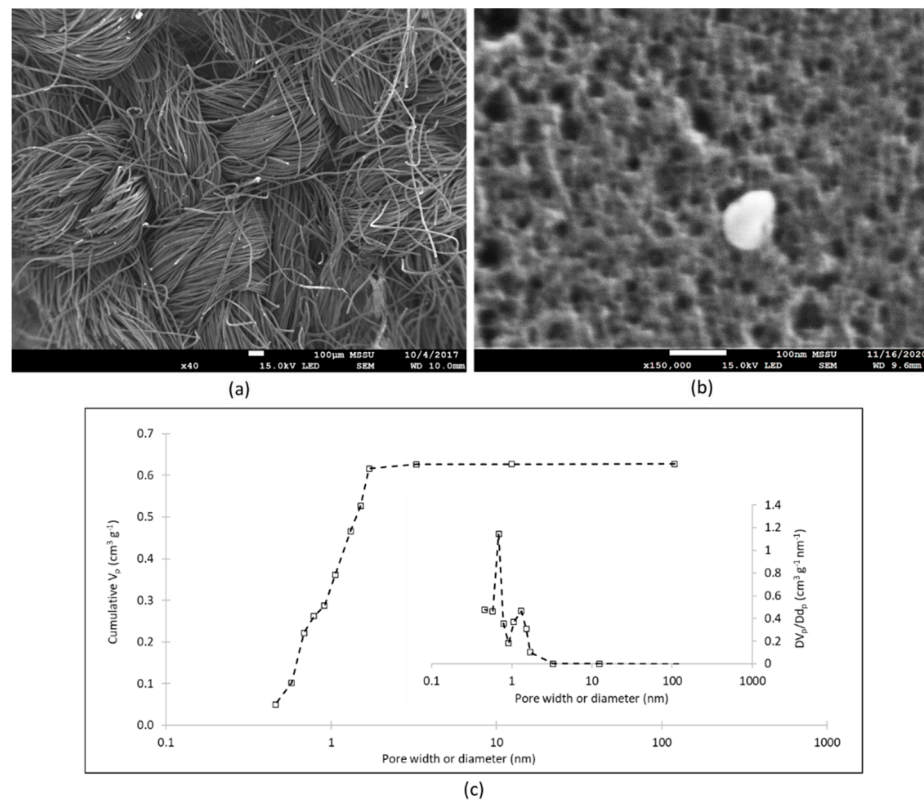


Figure 1. Cathode host: (a,b) SEM images of cathode host activated carbon fabric (ACF); (c) discretized pore size distribution (PSD) of cathode host ACF.

ACF samples of 1 cm^2 (12 mg) were placed on 1-cm^2 aluminum foil (of $30\text{-}\mu\text{m}$ thickness, utilized as current collector in the battery cathode). Twelve mg of sulfur powder was sprinkled on the free top surface of each ACF sample. The assembly was wrapped by a single layer of aluminum foil (to entrap any sulfur vapor as much as possible), taking care for the wrap not to touch the sulfur powder. Finally, each wrapped assembly was placed in a sealed pressure vessel from stainless steel of a circular base of 160-mm diameter and height of 110 mm, as illustrated in Figure 2a. The pressure vessel was placed on a hot plate for a specified period of time. Different experiments were carried out at three different hot-plate temperatures: $T_b = 150, 175,$ and $200 \text{ }^\circ\text{C}$. External temperature monitoring was carried out during each experiment using an infrared (IR) camera (Figure 2b). On the basis of the ideal gas law, a gauge pressure range of 0–0.6 bar was estimated, where the safety valve in the pressure vessel was set to 1 bar and was never reached, i.e., the safety valve did not open in any of the experiments. It must be mentioned that the dimensions of the pressure vessel were designed so if its base allocated a maximum number of eight samples, the estimated maximum gauge pressure was below the safety valve setting of 1 bar. After 40 min and after 2 h at T_b , followed by 12 h cooling to room temperature, the samples were removed from the vessel; the 40- and 120-min experiments were independent experiments, where the 2-h experiments were not interrupted. Each sample on the current collector foil was weighed before and after sulfur powder was added, as well as at the end of the specified period of sulfur infiltration processing. Samples were examined under scanning electron microscope HR-SEM JEOL-7100 F (JEOL Ltd., Tokyo, Japan) in terms of SEM and EDX (energy-dispersive X-ray spectroscopy).

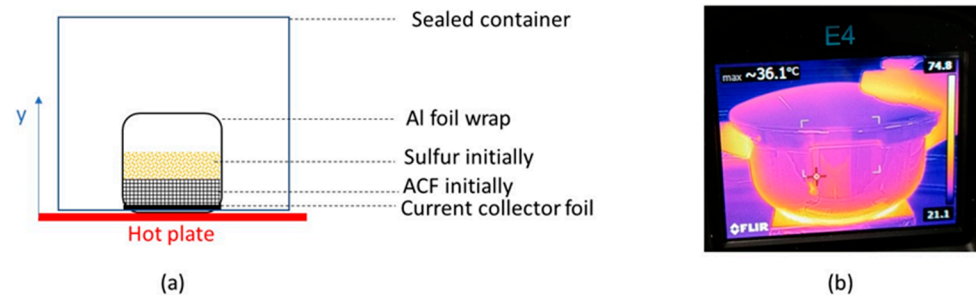


Figure 2. Sulfur impregnation setup: (a) assembly for the sulfur impregnation into ACF cathode host; y axis for the model in Section 3; (b) an infrared photograph from the temperature-monitoring procedure.

3. Modeling of the Sulfur Infiltration in the Porous Cathode Host

A numerical model was developed for the heat transfer and sulfur impregnation in the cathode host. On the basis of the diagram presented in Figure 2a, one-dimensional equations were assembled in the y-axis, given the small thickness of each component in the assembly.

All possible sulfur allotropes were considered for melt or low-temperature vapor [36] and the lowest energy structures were selected, as predicted by density functional theory (DFT) simulations by Jackson et al. [39]. Further molecular simulations were carried out in this study for geometrical optimization, using Avogadro, and the resulted molecular models are displayed in Figure 3a, together with the measured minimum dimension for each allotrope model and their formation energy, as calculated by Jackson et al. [39] employing DFT simulations. On the basis of the minimum dimension of each sulfur allotrope, it was deduced which allotrope may be accommodated in each pore size, as is presented for the peaks of the PSD of the porous cathode host ACF in Figure 3b. Pores smaller than 0.4 nm could not accommodate any sulfur in any form and pores smaller than 0.7 nm could not accommodate any sulfur in any form and pores smaller than 0.7 nm could not accommodate S_8 and S_7 .

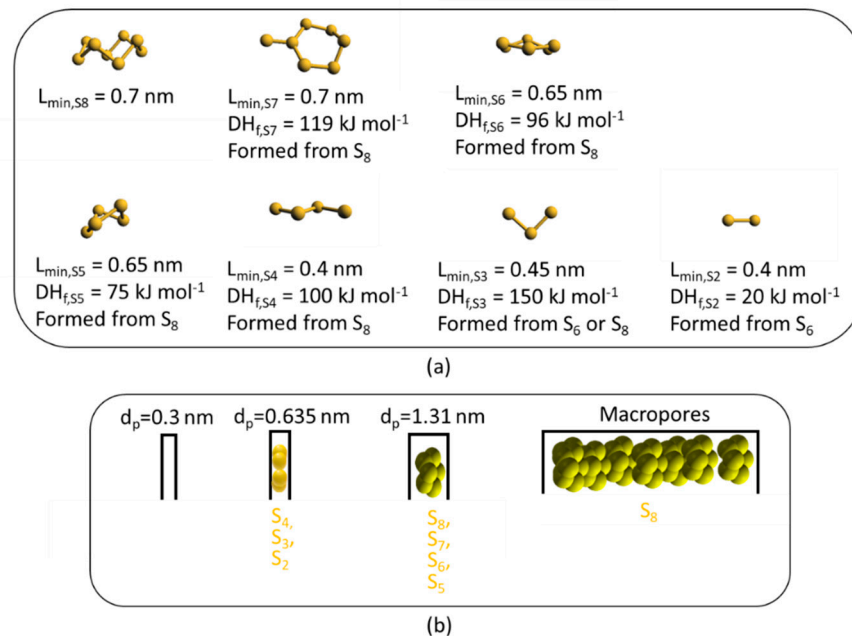


Figure 3. Sulfur allotropes in relation to pores in porous cathode host: (a) molecular models of sulfur allotropes, minimum dimension (L_{min}) for each allotrope and formation energy (DH_f) [39]; (b) possible accommodation of allotropes in different pore sizes (d_p), corresponding to the peaks of the PSD in Figure 1c.

The vertical assembly of different materials during the sulfur infiltration comprised from bottom to top (also see Figure 2a):

- (a) hot-plate specified temperature: T_b ;
- (b) pressure container wall from stainless steel ($\rho = 8000 \text{ kg m}^{-3}$; $c_p = 468 \text{ J kg}^{-1} \text{ K}^{-1}$; $k = 16.3 \text{ W m}^{-1} \text{ K}^{-1}$) of thickness of 3 mm;
- (c) aluminium foil of wrap ($\rho = 2725 \text{ kg m}^{-3}$; $c_p = 910 \text{ J kg}^{-1} \text{ K}^{-1}$; $k = 235 \text{ W m}^{-1} \text{ K}^{-1}$) of thickness of 30 μm ;
- (d) aluminium foil of current collector ($\rho = 2725 \text{ kg m}^{-3}$; $c_p = 910 \text{ J kg}^{-1} \text{ K}^{-1}$; $k = 235 \text{ W m}^{-1} \text{ K}^{-1}$) of thickness of 30 μm ;
- (e) ACF ($\rho = 240 \text{ kg m}^{-3}$; specific heat capacity in $\text{J kg}^{-1} \text{ K}^{-1}$ as a function of absolute temperature T : $c_p = 0.0004T + 0.8133$; $k = 0.12 \text{ W m}^{-1} \text{ K}^{-1}$) of thickness of 500 μm ;
- (f) ACF-sulfur composite consisting of ACF infiltrated with sulfur of varying thickness from 0 (non-infiltrated ACF) to 500 μm (fully infiltrated ACF);
- (g) sulfur layer of 12 mg cm^{-2} , consisting of initially solid S_8 allotrope ($\rho = 2070 \text{ kg m}^{-3}$; $c_p = 706 \text{ J kg}^{-1} \text{ K}^{-1}$; $k = 0.205 \text{ W m}^{-1} \text{ K}^{-1}$) which when melt ($\rho = 1819 \text{ kg m}^{-3}$; $c_p = 975 \text{ J kg}^{-1} \text{ K}^{-1}$; $k = 0.205 \text{ W m}^{-1} \text{ K}^{-1}$);
- (h) air layer (at temperature T (K) and pressure P (Pa): $\rho_{T,P} = 3.6 \times 10^{-3} P/T$ in kg m^{-3} ; $c_p = 1010 \text{ J kg}^{-1} \text{ K}^{-1}$; $k = 34 + 0.07(T - 273)$ in $\text{mW m}^{-1} \text{ K}^{-1}$) of thickness of 3 mm;
- (i) aluminium foil of wrap ($\rho = 2725 \text{ kg m}^{-3}$; $c_p = 910 \text{ J kg}^{-1} \text{ K}^{-1}$; $k = 235 \text{ W m}^{-1} \text{ K}^{-1}$) of thickness of 30 μm ;
- (j) air (at temperature T (K) and pressure P (Pa): $\rho_{T,P} = 3.6 \times 10^{-3} P/T$ in kg m^{-3} ; $c_p = 1010 \text{ J kg}^{-1} \text{ K}^{-1}$; $k = 34 + 0.07(T - 273)$ in $\text{mW m}^{-1} \text{ K}^{-1}$) of thickness of 100 mm;
- (k) pressure container ceiling from stainless steel ($\rho = 8000 \text{ kg m}^{-3}$; $c_p = 468 \text{ J kg}^{-1} \text{ K}^{-1}$; $k = 16.3 \text{ W m}^{-1} \text{ K}^{-1}$) of thickness of 3 mm.

The heat transfer equation for each single material layer, i , is given by:

$$\frac{\partial T}{\partial t} = \frac{k_i}{\rho_i c_{p,i}} \frac{\partial^2 T}{\partial y^2} - \sum_j R_j D H_{f,S_j} \tag{1}$$

where T is the temperature, t is the time, y is the vertical axis, ρ is density, c_p is specific heat capacity, k is thermal conductivity, subscript i denotes layer i , and $\sum_j R_j D H_{f,S_j}$ is the power lost due to the formation of new sulfur allotropes j . The air pressure in the container was updated according to the updated air temperature, employing the ideal gas law. The specific heat capacity of sulfur, $c_{p,S}$, is given as a function of the absolute temperature, T (in K), by the following relation with the values of the constants given in Table 1 [40].

$$c_{p,S} = \frac{a + bT + cT^2 + dT^3}{0.032} \tag{2}$$

Table 1. Density and heat capacity of sulfur [40].

Title 1	Solid S_8 Orthorhombic $T < 95 \text{ }^\circ\text{C}$	Solid S_8 Monoclinic $95 \text{ }^\circ\text{C} \leq T < 120 \text{ }^\circ\text{C}$	Melt Sulfur $120 \text{ }^\circ\text{C} \leq T < 159 \text{ }^\circ\text{C}$	Melt Sulfur $159 \text{ }^\circ\text{C} \leq T$
ρ_S (kg m^{-3})	2070	1960	1819	1819
a	21.22	21.22	-4540.97	-37.93
b	3.86	3.86	26,065.60	133.24
c	22.27	22.27	-55,520.70	-95.32
d	-10.32	-10.32	42,112.20	24.01

For the composite ACF-S, the thermal diffusivity, $\frac{k_i}{\rho_i c_{p,i}}$, is given by the rule of mixtures, where the thermal diffusivity of the sulfur is weighted by the volume fraction of the impregnated sulfur in the ACF. At the boundaries between adjacent layers, there is heat

flux continuity boundary condition, with a contact resistance, $1/h_c$, to take into account any non-perfect contact at the ACF/current collector interface and previous interfaces (layers (b)–(e)). A fixed boundary condition, T_b , is used at the bottom of layer (b), in contact with the hot plate. The time-changing temperature at the ceiling of the pressure container is given by the temperature at that height from the IR images, monitoring the experiment, and used as input data in the heat transfer simulation. A heat transfer coefficient of $390 \text{ W m}^{-2} \text{ K}^{-1}$ was used for the heat transfer via natural convection between the S-ACF and air [41,42] and of $2280 \text{ W m}^{-2} \text{ K}^{-1}$ between air and aluminum foil or stainless steel top plate [43].

At the sulfur melt–solid interface, with sulfur melt point at $119.7 \text{ }^\circ\text{C}$, there is the boundary condition:

$$\rho_{S,m} \Delta H_m \frac{\partial S_m}{\partial t} = k_{S,s} \frac{\partial T_s}{\partial y} - k_{S,m} \frac{\partial T_m}{\partial y} \quad (3)$$

where $\frac{\partial S_m}{\partial t}$ is the rate of sulfur melt generation, ΔH_m is the heat of fusion of sulfur, $\Delta H_m = 54 \text{ kJ kg}^{-1}$ [40], and, for the rest of properties, subscripts s and m denote solid and melt, respectively.

Sublimation (solid-to-vapor for temperatures below $119.7 \text{ }^\circ\text{C}$) and vaporization of sulfur (melt-to-vapor for temperatures above $119.7 \text{ }^\circ\text{C}$) occur from the top surface of sulfur layer (g) ((g) top subscript), where a heat flux loss occurs at that boundary with the air layer boundary (h), according to the relation:

$$\rho_{S,v} \Delta H_{S,v} \frac{\partial S_v}{\partial t} = k_{S,s \text{ or } m} \frac{\partial T_{(g)\text{top}}}{\partial y} - k_{S,v} \frac{\partial T_{(h)}}{\partial y} \quad (4)$$

where the heat of vaporization is $\Delta H_{S,v} = 306.25 \text{ kJ kg}^{-1}$ and the heat of sublimation is $\Delta H_{S,v} = 360.31 \text{ kJ kg}^{-1}$ [40]. The rate of generation of S vapor sulfur moles, $dN_{S,v}/dt$, is given by the equation [44,45]:

$$\frac{dN_{S,v}}{dt} = -A \frac{U_{\text{transfer}} P_{S,v}}{RT} \quad (5)$$

where A is the area of the top surface of layer (g), U_{transfer} is the mass transfer coefficient, $P_{S,v}$ is the sulfur vapor pressure and R is the gas constant $R = 8.3145 \text{ J mol}^{-1} \text{ K}^{-1}$. The mass transfer coefficient is given by the relation [45]:

$$U_{\text{transfer}} = \frac{1.5 D_{S,v}^{0.75} g^{0.25}}{(0.2 \mu_{S,v})^{0.25}} \quad (6)$$

where g is gravity ($g = 9.81 \text{ m s}^{-2}$), $\mu_{S,v}$ is the sulfur vapor viscosity given by the linear relation against temperature fitting the experimental data from [46], as presented in Figure 4a, and $D_{S,v}$ is the diffusion coefficient of the sulfur vapor, given as a function of temperature, T (in K), by the following relation [44], assuming binary coefficients with air being the second vapor-phase material [44]:

$$D_{S,v} = \frac{3.3 \times 10^{-3} T^{1.5}}{10^5 \left[\left(\frac{0.256}{\rho_{S,v}} \right)^{1/3} + \left(\frac{0.018}{\rho_{\text{air}}} \right)^{1/3} \right]^2} \quad (7)$$

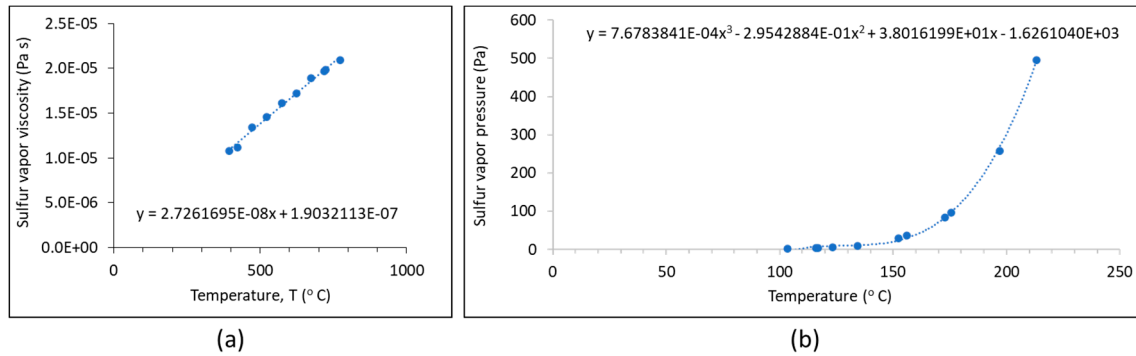


Figure 4. Data fits for sulfur vapor (a) linear fit of experimental data (data table from [46]) of sulfur vapor viscosity against temperature; (b) polynomial fit of experimental data (data table from [47]) of sulfur vapor pressure against temperature.

The sulfur vapor pressure is considered a function of temperature from the polynomial data fit of experimental data from [47], as is presented in Figure 4b.

The second system of equations describes the mass transport of each sulfur allotrope, S_j for $j = 2-8$ (Figure 3a), and infiltration through the porous ACF in the average y -axis and in each pore size, p , from the discretized PSD in Figure 1c:

$$\frac{\partial C_{j,p}}{\partial t} + F_{\text{decay},j,p} \frac{\partial u_p C_{j,p}}{\partial y} = F_{\text{decay},j,p} D_{j,p} \frac{\partial^2 C_{j,p}}{\partial y^2} + R_j - r_j \quad (8)$$

where $C_{j,p}$ is the concentration of sulfur allotrope j in pore size p , u_p is the velocity in pore size p , $D_{j,p}$ is the diffusion coefficient of sulfur allotrope j in pore size p , R_j is the rate of formation of new allotrope S_j in pore size d_p , r_j is the rate of loss of allotrope S_j due to the formation of lower order allotropes for smaller pores, and $F_{\text{decay},p}$ is a decay factor where $F_{\text{decay},j,p} = 1$ for the S_8 allotrope ($j = 8$) but depends on local thermal energy and allotrope formation energy for the lower order sulfur allotropes.

Parallel infiltration paths are considered for the different pore sizes, with the mean velocity, u_p , for each pore size calculated according to Darcy’s law in the same manner as matrix infiltration in a fibrous medium in composites’ manufacturing [37,48]:

$$u_p = \frac{K_p}{\epsilon_p \mu_{S,m}} \frac{\partial P_{c,p}}{\partial L_f} \quad (9)$$

where ϵ_p is the pore fraction for pores sized p , L_f is the filled length across the thickness of the porous ACF, K_p is the permeability of the porous medium for pore size d_p given by the Carman–Kozeny equation for flow transverse to fibers with Kozeny constant of 3.4 [49]:

$$K_p = \frac{\epsilon_p d_p^2}{4 \times 3.4} \quad (10)$$

$P_{c,p}$ is the capillary pressure given by the Young–Laplace equation [37,50]:

$$P_{c,p} = \frac{2\sigma \cos \theta}{d_p} \quad (11)$$

where σ is the surface tension of the infiltrating sulfur fluid, θ is its contact angle with the carbon pore walls ($\sigma = 61 \text{ mN m}^{-1}$ and $\theta = 4.3^\circ$ [51] in this study), and $\mu_{S,m}$ is the viscosity of the sulfur melt, its value taken from experimental data depending on temperature [33] as:

$$\begin{aligned} 119.7 \text{ }^\circ\text{C} \leq T < 165 \text{ }^\circ\text{C}: \mu_{S,m} &= 0.04 \text{ Pa s} \\ 165 \text{ }^\circ\text{C} \leq T < 185 \text{ }^\circ\text{C}: \mu_{S,m} &= 0.035 \text{ Pa s} \\ 185 \text{ }^\circ\text{C} \leq T < 195 \text{ }^\circ\text{C}: \mu_{S,m} &= 0.92 \text{ Pa s} \\ 195 \text{ }^\circ\text{C} \leq T: \mu_{S,m} &= 0.85 \text{ Pa s} \end{aligned} \quad (12)$$

Sulfur allotropes are generated (R_j) and infiltrate the pores in pore size hierarchy, as follows. All pores with $d_p \geq L_{\min,S8}$ are infiltrated by the S_8 allotrope. Pores with $L_{\min,S8} > d_p \geq L_{\min,S7}$ are first given the chance to be infiltrated with the S_7 allotrope, if there is sufficient local thermal energy, E_{Th} , available to overcome the formation energy of S_7 , $DH_{f,S7}$. Otherwise, formation and infiltration of S_6 is considered and consecutive smaller allotropes, pores with $L_{\min,S7} > d_p \geq L_{\min,S6}$, are first given the chance to be infiltrated with the S_6 allotrope, if there is sufficient local thermal energy available to overcome the formation energy of S_6 , $DH_{f,S6}$. Otherwise, formation and infiltration of S_5 is considered and consecutive smaller allotropes. The procedure continues in the same manner until pores of $d_p < L_{\min,S2}$ are encountered, which cannot be infiltrated by any form of sulfur. The rate of formation of a sulfur allotrope, R_j , encompasses the full concentration of the parent allotrope (Figure 3a) for that pore size, multiplied by the decay factor, $F_{\text{decay},j,p}$, given by the equation [24]:

$$F_{\text{decay},j,p} = e^{-\left(\frac{DE_{f,Sj}}{RT+E_{Th}}\right)} \quad (13)$$

The diffusion coefficient of sulfur allotrope j in pore size d_p is given by the following relation [17] (where k_B is Boltzmann's constant), which is a modified Einstein's equation to take into account tortuosity and constrictivity effects [24]:

$$D_{j,p} = \frac{\varepsilon_p^{1.5} k_B T}{2\pi\mu_{S,m} L_{\min,Sj}} \left(1 - \frac{L_{\min,Sj}}{d_p}\right)^4 \quad (14)$$

The system of the heat transfer and sulfur transport equations was solved using the implicit time-dependent finite volume/finite difference technique [52,53]. Computer simulations were performed for the experimental process described in Section 2, at $T_b = 150^\circ\text{C}$ or 175°C or 200°C for two alternative, specified infiltration durations: 40 min or 2 h, employing a timestep $\Delta t = 0.1$ s and a y -increment $\Delta y = 5 \mu\text{m}$ in layers (a)–(i).

4. Results

The monitoring IR camera showed that after the hot plate reached the set temperature and the steel container with the samples was placed on the hot plate, the hot-plate temperature was disturbed and it took about 30–40 min to reach the set temperature again. From then on, the samples were left for sulfur infiltration for either 40 min or 2 h. To ensure that the correct experimental temperature profile was used, both the bottom and top temperatures of the steel container were inputted in the computer simulations from the monitoring IR camera. For hot plate-temperature $T_b = 150^\circ\text{C}$, the sulfur powder did not melt and was still on top of the ACF samples when the steel container was opened, after either 40 min or 2 h. The computational simulations predicted an end, steady-state temperature of 109.88°C at the top of the ACF sample, which was below the sulfur melting temperature, which justified the experimental result.

The computational simulations predicted an end, steady-state temperature of 125.55°C and 146.8°C at the top of the sulfur layer for initially set, experimental hot-plate temperatures of 175°C and 200°C , respectively. These steady state temperatures at the top of ACF were then above the sulfur melting point.

Figure 5 displays the predicted total mass of sulfur (in the form of any allotrope) that infiltrated the porous ACF and also and in top sulfur layer as a function of the infiltration time, for the two, set, hot-plate temperatures, 175°C and 200°C . It also compares the predictions with the experimental data of the weight gain after sulfur infiltration of 40 min and 2 h. Initially, the sulfur was approximately 12 mg cm^{-2} , same as the amount of sulfur added initially. Sulfur evaporation or sublimation seemed to start slowly and then accelerated as the sample was heated and continued until the sulfur started impregnating meso- and micropores, where the numerical model considered that it was trapped without vapor escape from the ACF. In the simulations, sulfur seemed to impregnate and stay in the macropores for longer in the samples at set, hot-plate temperature, $T_b = 175^\circ\text{C}$, from which

it may have evaporated faster due to the larger surface area of macropores, compared with the assumed flat surface of the sulfur layer at the top of ACF. Hence, there was faster initial sulfur evaporation for $T_b = 175\text{ }^\circ\text{C}$, compared to the samples at $T_b = 200\text{ }^\circ\text{C}$. However, overall, more sulfur evaporated until the end for the samples at $T_b = 200\text{ }^\circ\text{C}$, which was attributed to the higher temperature resulting in higher vapor pressure, as seen in Figure 4b. As a result, the set hot-plate temperature $T_b = 175\text{ }^\circ\text{C}$ is recommended, provided that the sulfur is distributed homogeneously through the thickness of the ACF sample and there is no accumulated sulfur layer at the top or bottom surface on the sample. This was investigated, both in the predictions and experimentally, in the rest of this study.

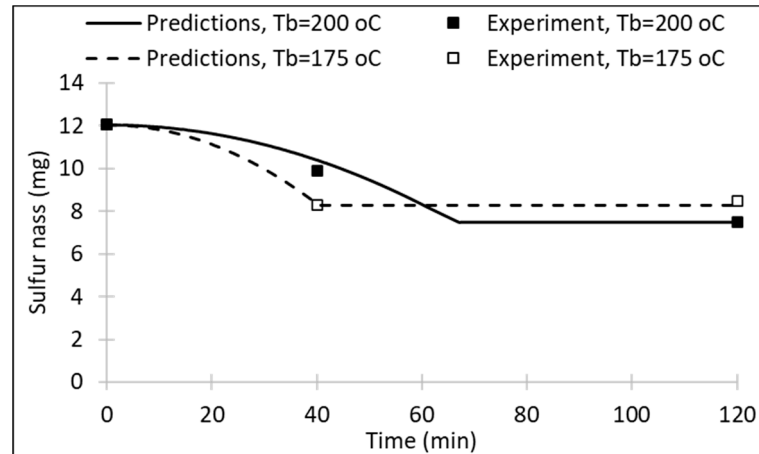


Figure 5. Predicted total mass of sulfur in ACF and top sulfur layer as a function of time and comparison with the experimental data at 40 and 120 min; error bars in the experimental data points from five repeat experiments.

Figures 6 and 7 present the SEM/EDX element maps of sulfur and carbon of the top surface and cross section, respectively, of ACF samples after being impregnated with sulfur for 40 and 120 min for set, hot-plate temperature $T_b = 200$ or $175\text{ }^\circ\text{C}$. In general, it can be seen that there was no sulfur present in the interfiber space and the sulfur impregnated very well the AC fibers. The cross sections in Figure 7 are from samples cut after their sulfur impregnation. Figure 7 illustrates that sulfur impregnated homogeneously across the whole thickness of the sample, without any accumulation at the top or the bottom of the sample. No leftover, unimpregnated sulfur was detected in any of the case studies: $T_b = 200$ or $175\text{ }^\circ\text{C}$, impregnation time 40 or 120 min. The cross section of one of the cut fibers of Figure 7b is presented in Figure 8, where S, C, and mixed S/C element maps depict that there was no sulfur layer surrounding the carbon fiber and, in fact, the sulfur had higher concentration in the central region of the fiber drawn by capillary flow into the micropores there. Any sulfur and carbon in the background of the fiber in Figure 8 was from the neighboring fibers, as shown in Figure 7b.

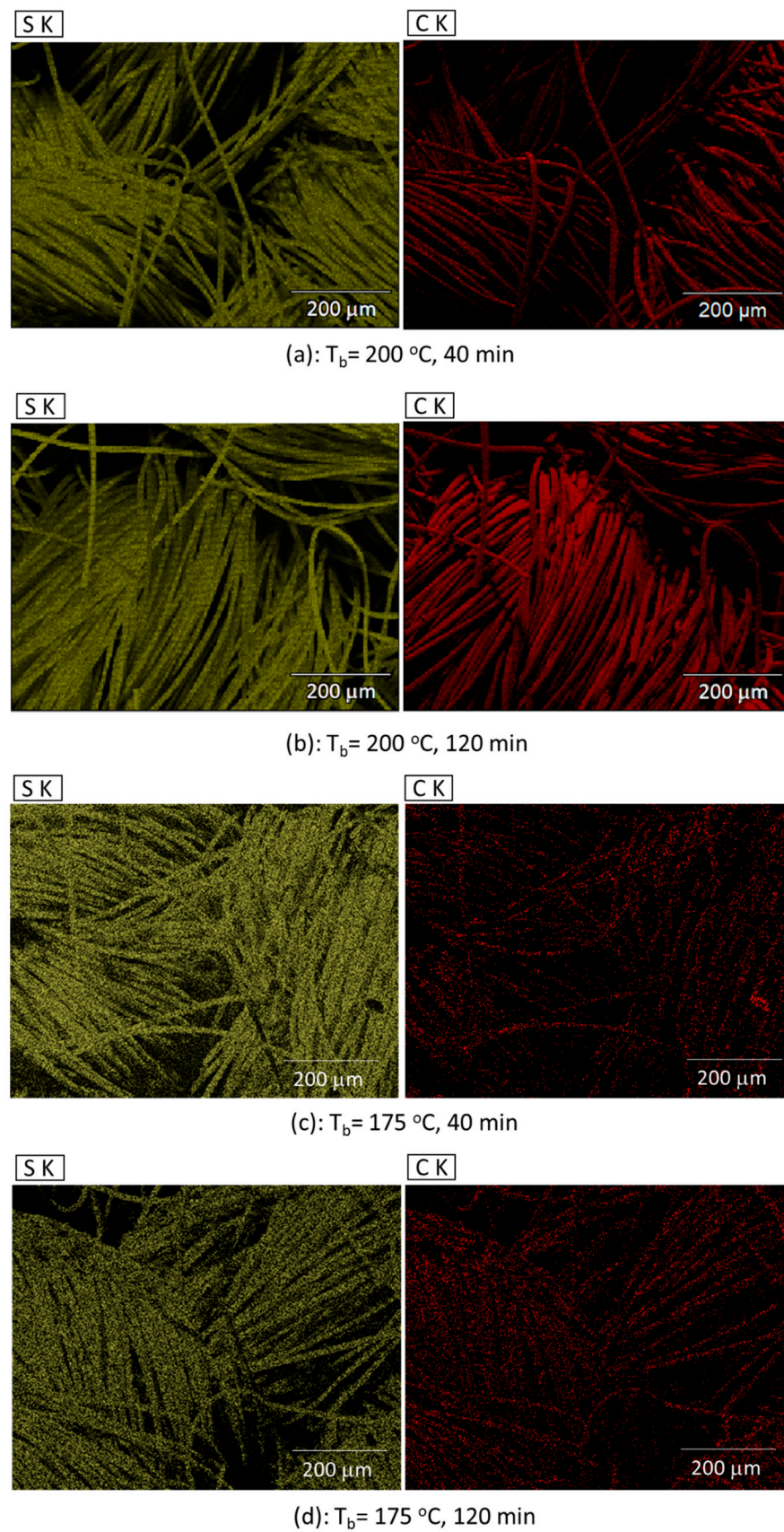


Figure 6. SEM/EDX element maps of sulfur (yellow) and carbon (red) of the top surface of the ACF samples impregnated with sulfur; each set of S/C element maps is from a different sample.

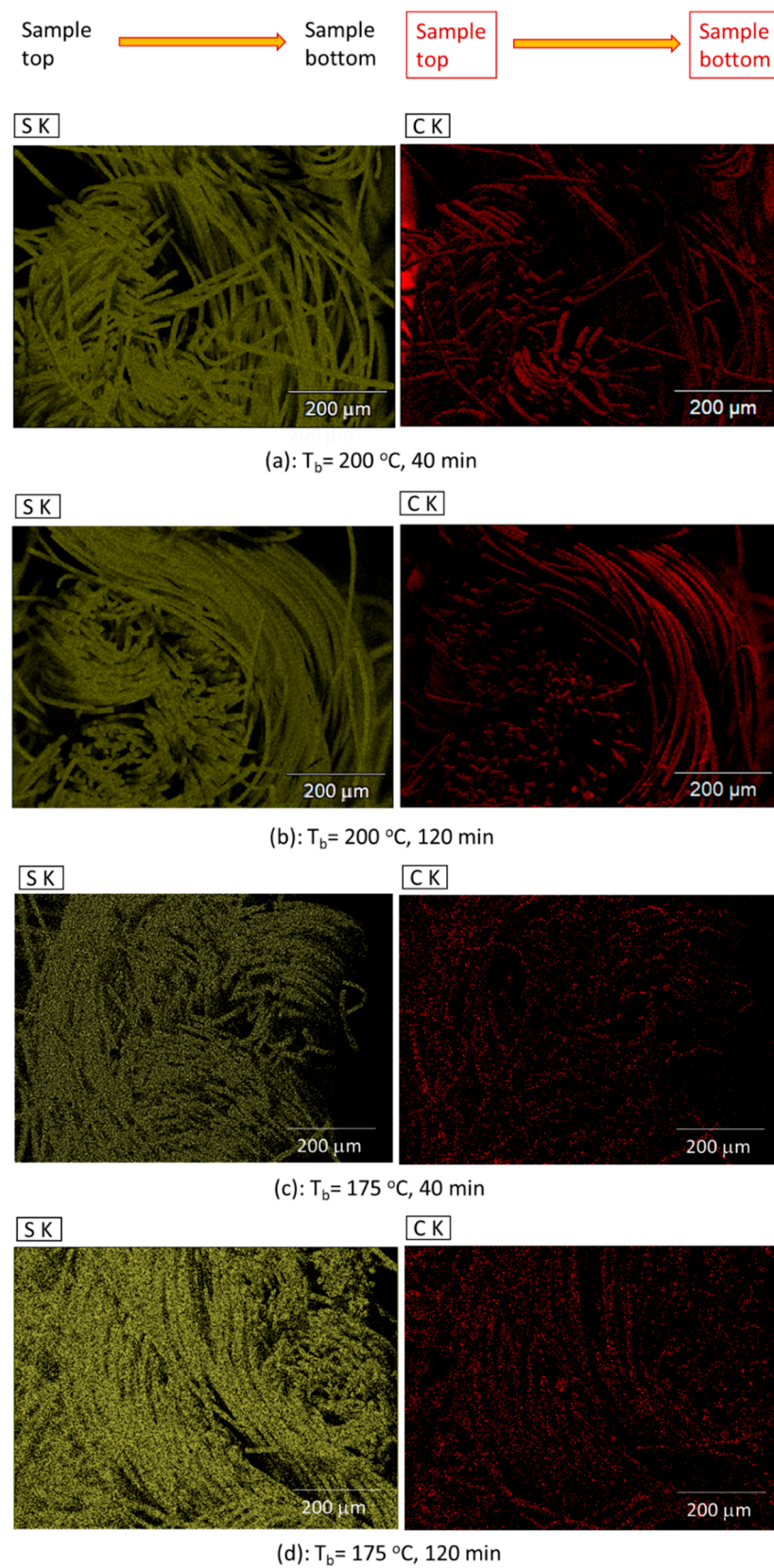


Figure 7. SEM/EDX element maps of sulfur (yellow) and carbon (red) of the cross section of the ACF samples impregnated with sulfur, where, in each image, left to right represents top-to-bottom direction in the sample; each set of S/C element maps is from a different sample.

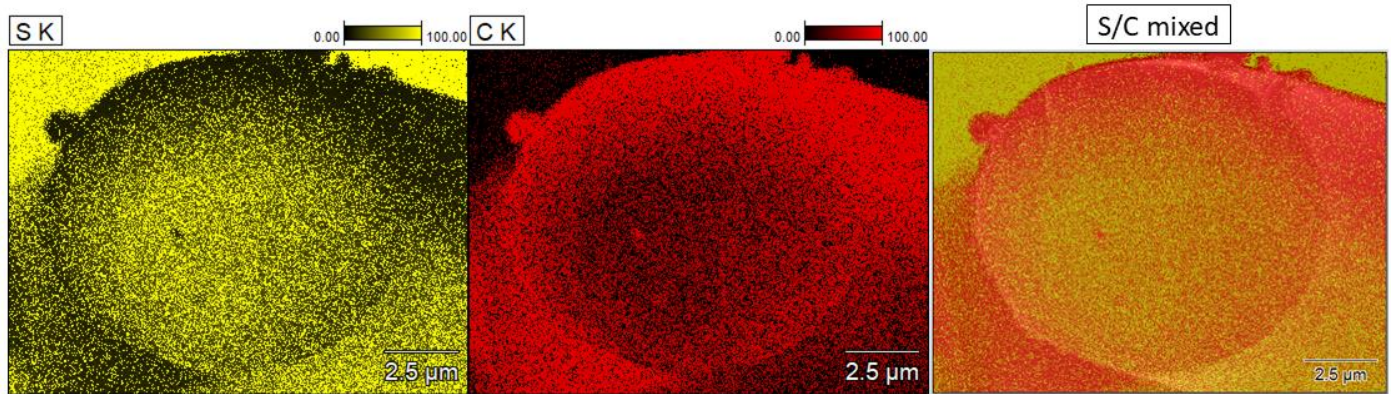


Figure 8. SEM/EDX element maps of sulfur (yellow) and carbon (red) and a mixed S/C element map of the cross section of an activated carbon (AC) fiber impregnated with sulfur, from magnification of sample image of Figure 7b.

Figure 9 presents the predicted evolution of different sulfur allotropes near the bottom of the ACF. Sulfur infiltration took place in a hierarchical manner, where the large pores were infiltrated first, followed by mesopores and, lastly, by micropores. S_8 entered rapidly and hierarchically the large pores that could accommodate it, i.e., $d_p > 0.7$ nm. For pores smaller than 0.7 nm, S_8 converted to S_6 , and then to S_4 for $d_p < 0.65$ nm.

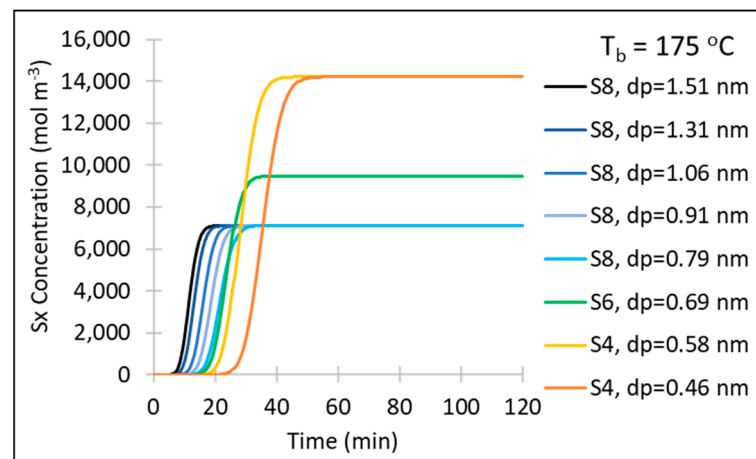


Figure 9. Predicted evolution of the concentration of the sulfur allotropes in different pore sizes in the ACF (near the bottom surface of ACF) as a function of time.

Figure 10 presents the predicted contour plots of the sulfur concentration at the end of the 40 min and the 2 h infiltration periods, for set hot-plate temperature $T_b = 175$ °C. Micropores greater than 0.7 nm were impregnated with S_8 . Pores smaller than 0.8 nm and larger than 0.6 nm contained S_6 , and pores smaller than 0.64 nm and larger than 0.4 nm contained S_4 . The sulfur distribution was homogeneous through the ACF thickness at the end of the 2 h infiltration period. After 40 min sulfur infiltration, there was some low S_8 concentration in the meso- and macropores near the top ACF surface, which was depleted in the subsequent infiltration time for the sulfur infiltration into the lower parts, while the initial top reservoir of sulfur over the ACF was exhausted. At the end of the 40 min infiltration period, S_4 had not fully infiltrated yet the bottom 20% of the ACF but the S_4 infiltration was completed through the whole ACF thickness at the end of the 2-h period.

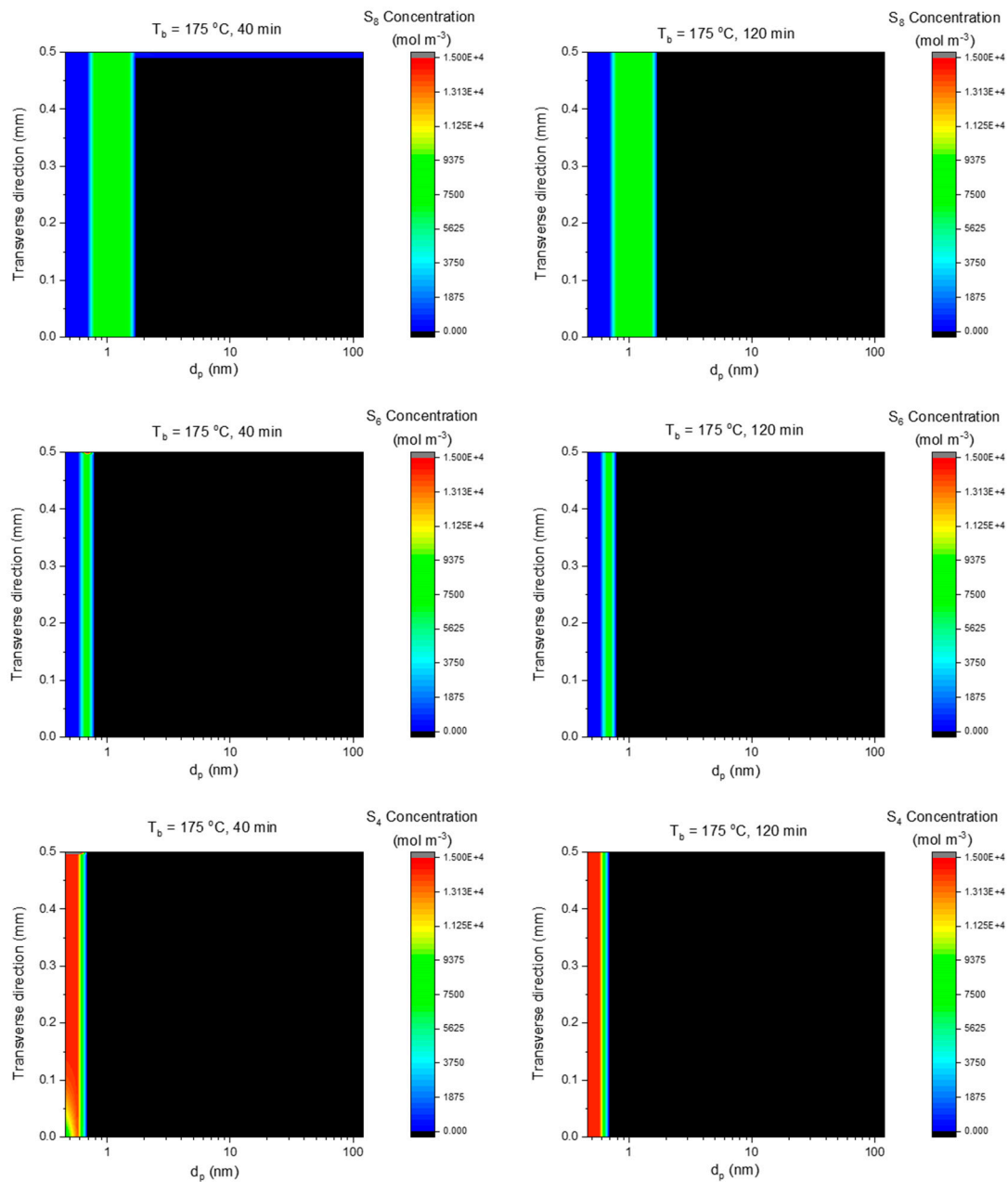


Figure 10. Predicted contour plots of the concentration of different sulfur allotropes after 40 min and after 2 h of infiltration time, as a function of the pore diameter and vertical position in the sulfur-ACF composite cathode, where $y = 0$ at current collector and $y = 0.5$ mm at the top of the composite cathode.

5. Discussion

It is most interesting that in both the experiment and the computational simulation a sulfur loss of 59–62 wt% occurred, depending on hot-plate temperature. Sulfur vapor may have escaped outside the aluminum wrap, as after several such experiments the inner walls of the stainless steel pressure vessel obtained a shiny, yellowish hue. The heat transfer characteristics of the experimental rig greatly affected the temperature distribution and, hence, sulfur vaporization and also infiltration. Alternative experimental setups in the literature include sulfur impregnation with the sample in a convection oven [12] where, in fact, even higher degree of sulfur vaporization was observed [12]. The methodology of a sealed container on a hot plate with set hot-plate temperature, employed in this study, may represent continuous, large-scale sulfur deposition on a substrate tape moving continually on a conveyor belt. The substrate may be ACF on aluminum foil current collector, their

assembly moving on the conveyor belt with sulfur powder being sprayed on top and the bed of the moving belt being heated to the set temperature. Hence, the heat transfer and sulfur infiltration model presented in this study is applicable to a scaled fabrication of composite S-ACF cathode. As sulfur loss through vaporization and sublimation is generally undesirable, process design simulations may try to optimize the temperature and external pressure to maintain sulfur infiltration in melt state rather than vapor state. This would mean that only S_8 allotrope would be present, as lower-order sulfur allotropes are formed in vapor state only. As a result, cathode host micropores below 0.7 nm would not contain any sulfur and such unfilled pores would, instead, absorb and waste the electrolyte solvent of the Li-S battery without any prospect of active participation in the redox battery reactions in the absence of sulfur.

It was predicted that in pores smaller than 0.7 nm (and greater than 0.4 nm) the sulfur resides in the form of mainly S_6 and S_4 allotropes. The so confined sulfur in small carbon micropores cannot move to the anode so easily in a Li-S battery, which offers the advantage of limiting the “shuttling” effect in the Li-S battery [54].

However, S_4 in micropores smaller than 0.64 nm, which occupy 16% of the total volume of pores sized 0.46–119 nm in the ACF of this study, reduces the capacity of the first potential plateau at 2.3–2.4 V in the discharge of a Li-S battery for some composite cathodes, as this plateau corresponds to the conversion of Li_2S_8 to Li_2S_6 [5,54]. Therefore, it can be seen that the pore size distribution of the porous carbon host is critical for both the amount and form of infiltrated sulfur, which are going to affect the capacity of the Li-S battery, depending on the amount and allotrope type of sulfur and its energy stored and delivered, which depends on the integrated product of potential and capacity.

Hence, the design of future cathode hosts for Li-S batteries is a complex exercise. Micropores smaller than 0.7 nm are detrimental for the Li-S battery energy, as they can only accommodate lower-order sulfides that reduce the first voltage plateau in the battery while these micropores consume electrolyte, which is sometimes a waste as the absorbed electrolyte remains passive if there is no sufficient sulfur to utilize it in redox reactions. However, these pores filled with the electrolyte offer a high-power supercapacitor component and the device is then a hybrid Li-S battery/Li-ion capacitor. Furthermore, larger micropores might be beneficial to the Li-S battery as they can accommodate S_8 and restrict escape of polysulfides, reducing the “shuttling” effect during battery cycling.

The numerical model of heat transfer and sulfur infiltration outlined in this paper may also be applied to other porous cathode hosts, such as activated carbon powder [7,9,10] graphene [11,12] or other porous carbon material [6] with measured pore size distribution that can be used as input data in the simulations. The material properties and porosity would be used to determine the thermal properties (heat capacity and thermal conductivity) for the heat transfer, Equation (1). The pore size distribution of the porous host controls the sulfur impregnation in Equations (8)–(11) and the type of sulfur allotrope that may be formed in each pore size. In general, simulations of the sulfur infiltration may comprise the first stage, in a comprehensive numerical model of cathode fabrication and Li-S battery operation. Combining simulations of the composite cathode fabrication and battery cycling will help in the design of optimized porous hosts and composite cathodes.

6. Conclusions

The pore size distribution of a porous carbon host for a composite cathode is very important in a Li-S battery, both in cathode manufacture and during battery operation. A numerical model has been developed in this study for the description of the sulfur infiltration into the porous host while heated above the melting point of sulfur in cathode manufacture, taking into account the pore size distribution of the porous host and including heat transfer, sulfur sublimation, and evaporation, as well as formation of lower-order sulfur allotropes, depending on pore size and available thermal energy compared to their energy of formation. Computational simulations predicted a composite cathode with 38 and 41 wt% sulfur for set hot-plate temperatures of 200 and 175 °C, respectively, with

homogeneous sulfur distribution through the ACF thickness after 2 h of infiltration. In terms of the porous carbon host, pores smaller than 0.4 nm could not accommodate any sulfur allotrope. For pores smaller than 0.7 nm, sulfur resided mainly in the form of S₄ and of S₆. S₈ resided in micropores between 0.7 and 1.5 nm.

Author Contributions: Conceptualization, C.L.; methodology, K.L., J.P.B., and C.L.; software, K.L. and C.L.; validation, K.L. and J.P.B.; formal analysis, K.L., J.P.B., and C.L.; investigation, K.L., J.P.B., and C.L.; resources, C.L.; data curation, C.L.; writing—original draft preparation, K.L. and C.L.; writing—review and editing, C.L.; visualization, K.L., J.P.B., and C.L.; supervision, C.L.; project administration, C.L. All authors have read and agreed to the published version of the manuscript.

Funding: J.P.B. gratefully acknowledges funding from EPSRC project HiPoBat.

Conflicts of Interest: The authors declare no conflict of interest.

References

1. Zhu, K.; Wang, C.; Chi, Z.; Ke, F.; Yang, Y.; Wang, A.; Wang, W.; Miao, L. How far away are lithium-sulfur batteries from commercialization? *Front. Energy Res.* **2019**, *7*, 123. [[CrossRef](#)]
2. Reddy, M.V.; Mauger, A.; Julien, C.M.; Paoletta, A.; Zaghbi, K. Brief history of early lithium-battery development. *Materials* **2020**, *13*, 1884. [[CrossRef](#)] [[PubMed](#)]
3. Reddy, M.V.; Subba Rao, G.V.; Chowdari, B.V.R. Metal oxides and oxysalts as anode materials for li ion batteries. *Chem. Rev.* **2013**, *113*, 5364–5457. [[CrossRef](#)] [[PubMed](#)]
4. Petnikota, S.; Rotte, N.K.; Srikanth, V.V.S.S.; Kota, B.S.R.; Reddy, M.V.; Loh, K.P.; Chowdari, B.V.R. Electrochemical studies of few-layered graphene as an anode material for Li ion batteries. *J. Solid State Electrochem.* **2014**, *18*, 941–949. [[CrossRef](#)]
5. Elazari, R.; Salitra, G.; Garsuch, A.; Panchenko, A.; Aurbach, D. Sulfur-impregnated activated carbon fiber cloth as a binder-free cathode for rechargeable Li-S batteries. *Adv. Mater.* **2011**, *23*, 5641–5644. [[CrossRef](#)] [[PubMed](#)]
6. Ji, X.; Lee, K.T.; Nazar, L.F. A highly ordered nanostructured carbon–sulphur cathode for lithium–sulphur batteries. *Nat. Mater.* **2009**, *8*, 500–506. [[CrossRef](#)]
7. Xu, G.; Ding, B.; Nie, P.; Shen, L.; Dou, H.; Zhang, X. Hierarchically porous carbon encapsulating sulfur as a superior cathode material for high performance lithium–sulfur batteries. *ACS Appl. Mater. Interfaces* **2014**, *6*, 194–199. [[CrossRef](#)] [[PubMed](#)]
8. Kim, J.; Lee, D.-J.; Jung, H.-G.; Sun, Y.-K.; Hassoun, J.; Scrosati, B. An advanced lithium-sulfur battery. *Adv. Funct. Mater.* **2013**, *23*, 1076–1080. [[CrossRef](#)]
9. Vijayan, B.L.; Misnon, I.I.; Kumar, G.M.A.; Miyajima, K.; Reddy, M.V.; Zaghbi, K.; Karuppiah, C.; Yang, C.-C.; Jose, R. Facile fabrication of thin metal oxide films on porous carbon for high density charge storage. *J. Colloid Interface Sci.* **2020**, *562*, 567–577. [[CrossRef](#)]
10. Vijayan, B.L.; Zain, N.K.M.; Misnon, I.I.; Reddy, M.V.; Adams, S.; Yang, C.-C.; Anilkumar, G.M.; Jose, R. Void space control in porous carbon for high-density supercapacitive charge storage. *Energy Fuels* **2020**, *34*, 5072–5083. [[CrossRef](#)]
11. Ji, L.; Rao, M.; Zheng, H.; Zhang, L.; Li, Y.; Duan, W.; Guo, J.; Cairns, E.J.; Zhang, Y. Graphene oxide as a sulfur immobilizer in high performance lithium/sulfur cells. *J. Am. Chem. Soc.* **2011**, *133*, 18522–18525. [[CrossRef](#)]
12. Reece, R.; Lekakou, C.; Smith, P.A.; Grilli, R.; Trapalis, C. Sulphur-linked graphitic and graphene oxide platelet-based electrodes for electrochemical double layer capacitors. *J. Alloys Compd.* **2019**, *792*, 582–593. [[CrossRef](#)]
13. Di Lecce, D.; Marangon, V.; Du, W.; Brett, D.J.L.; Shearing, P.R.; Hassoun, J. The role of synthesis pathway on the microstructural characteristics of sulfur-carbon composites: X-ray imaging and electrochemistry in lithium battery. *J. Power Source* **2020**, *472*, 228424. [[CrossRef](#)]
14. Markoulidis, F.; Todorova, N.; Grilli, R.; Lekakou, C.; Trapalis, C. Composite electrodes of activated carbon and multiwall carbon nanotubes decorated with silver nanoparticles for high power energy storage. *J. Compos. Sci.* **2019**, *3*, 97. [[CrossRef](#)]
15. Markoulidis, F.; Lei, C.; Lekakou, C. Investigations of activated carbon fabric-based supercapacitors with different interlayers via experiments and modelling of electrochemical processes of different timescales. *Electrochim. Acta* **2017**, *249*, 122–134. [[CrossRef](#)]
16. Lei, C.; Markoulidis, F.; Wilson, P.; Lekakou, C. Phenolic carbon cloth-based electric double-layer capacitors with conductive interlayers and graphene coating. *J. Appl. Electrochem.* **2016**, *46*, 251–258. [[CrossRef](#)]
17. Lei, C.; Lekakou, C. Activated carbon–carbon nanotube nanocomposite coatings for supercapacitor application. *Surf. Coat. Technol.* **2013**, *232*, 326–330. [[CrossRef](#)]
18. Vermisoglou, E.C.; Giannakopoulou, T.; Romanos, G.; Giannouri, M.; Boukos, N.; Lei, C.; Lekakou, C.; Trapalis, C. Effect of hydrothermal reaction time and alkaline conditions on the electrochemical properties of reduced graphene oxide. *Appl. Surf. Sci. Part A* **2015**, *358*, 100–109. [[CrossRef](#)]
19. Vermisoglou, E.C.; Giannakopoulou, T.; Romanos, G.E.; Boukos, N.; Giannouri, M.; Lei, C.; Lekakou, C.; Trapalis, C. Non-activated high surface area expanded graphite oxide for supercapacitors. *Appl. Surf. Sci. Part A* **2015**, *358*, 110–121. [[CrossRef](#)]
20. Todorova, N.; Giannakopoulou, T.; Boukos, N.; Vermisoglou, E.; Lekakou, C.; Trapalis, C. Self-propagating solar light reduction of graphite oxide in water. *Appl. Surf. Sci. Part B* **2017**, *391*, 601–608. [[CrossRef](#)]

21. Vermisoglou, E.C.; Giannakopoulou, T.; Romanos, G.; Boukos, N.; Psycharis, V.; Lei, C.; Lekakou, C.; Petridis, D.; Trapalis, C. Graphene-based materials via benzidine-assisted exfoliation and reduction of graphite oxide and their electrochemical properties. *Appl. Surf. Sci.* **2017**, *392*, 244–255. [[CrossRef](#)]
22. Markoulidis, F.; Lei, C.; Lekakou, C. Fabrication of high-performance supercapacitors based on transversely oriented carbon nanotubes. *Appl. Phys. A Mater. Sci. Process.* **2013**, *111*, 227–236. [[CrossRef](#)]
23. Lekakou, C.; Moudam, O.; Markoulidis, F.; Andrews, T.; Watts, J.F.; Reed, G.T. Carbon-based fibrous EDLC capacitors and supercapacitors. *J. Nanotechnol.* **2011**, *2011*, 409382. [[CrossRef](#)]
24. Markoulidis, F.; Bates, J.; Lekakou, C.; Slade, R.; Laudone, G.M. Supercapacitors with lithium-ion electrolyte: An experimental study and design of the activated carbon electrodes via modelling and simulations. *Carbon* **2020**, *164*, 422–434. [[CrossRef](#)]
25. Fields, R.; Lei, C.; Markoulidis, F.; Lekakou, C. The Composite supercapacitor. *Energy Technol.* **2016**, *4*, 517–525. [[CrossRef](#)]
26. Lei, C.; Fields, R.; Wilson, P.; Lekakou, C.; Amini, N.; Tennison, S.; Perry, J.; Gosso, M.; Martorana, B. Development and evaluation of a composite supercapacitor-based 12 V transient start-stop (TSS) power system for vehicles: Modelling, design and fabrication scaling up. *Proc. Inst. Mech. Eng. Part A J. Power Energy* **2020**. [[CrossRef](#)]
27. Vermisoglou, E.C.; Giannouri, M.; Todorova, N.; Giannakopoulou, T.; Lekakou, C.; Trapalis, C. Recycling of typical supercapacitor materials. *Waste Manag. Res.* **2016**, *34*, 337–344. [[CrossRef](#)]
28. Kampouris, E.M.; Papaspyrides, C.D.; Lekakou, C.N. A model recovery process for scrap polystyrene foam by means of solvent systems. *Conserv. Recycl.* **1987**, *10*, 315–319. [[CrossRef](#)]
29. Kampouris, E.M.; Papaspyrides, C.D.; Lekakou, C.N. A model process for the solvent recycling of polystyrene. *Polym. Eng. Sci.* **1988**, *28*, 534–537. [[CrossRef](#)]
30. Muruges, A.K.; Uthayanan, A.; Lekakou, C. Electrophoresis and orientation of multiple wall carbon nanotubes in polymer solution. *Appl. Phys. A Mater. Sci. Process.* **2010**, *100*, 135–144. [[CrossRef](#)]
31. Bhargav, A.; He, J.; Gupta, A.; Manthiram, A. Lithium-sulfur batteries: Attaining the critical metrics. *Joule* **2020**, *4*, 285–291. [[CrossRef](#)]
32. Borchardt, L.; Oschatz, M.; Kaskel, S. Carbon materials for lithium sulfur batteries—Ten critical questions. *Chem. Eur. J.* **2016**, *22*, 7324–7351. [[CrossRef](#)]
33. Sofekun, G.O.; Evoy, E.; Lesage, K.L.; Chou, N.; Marriott, R.A. The rheology of liquid elemental sulfur across the λ -transition. *J. Rheol.* **2018**, *62*, 469–476. [[CrossRef](#)]
34. Tucker, R.P. Notes on the sublimation of sulfur between 25° and 50 °C. *Ind. Eng. Chem.* **1929**, *21*, 44–47. [[CrossRef](#)]
35. Carter, R.; Oakes, L.; Muralidharan, N.; Pint, C.L. Isothermal sulfur condensation into carbon scaffolds: Improved loading, performance, and scalability for lithium–sulfur battery cathodes. *J. Phys. Chem. C* **2017**, *121*, 7718–7727. [[CrossRef](#)]
36. Meyer, B. Elemental sulfur. *Chem. Rev.* **1976**, *76*, 367–388. [[CrossRef](#)]
37. Amico, S.; Lekakou, C. Flow through a two-scale porosity, oriented fibre porous medium. *Transp. Porous Media* **2004**, *54*, 35–53. [[CrossRef](#)]
38. Boukhalfa, S.; Gordon, D.; He, L.; Melnichenko, Y.B.; Nitta, N.; Magasinski, A.; Yushin, G. In situ small angle neutron scattering revealing ion sorption in microporous carbon electrical double layer capacitors. *ACS Nano* **2014**, *8*, 2495–2503. [[CrossRef](#)] [[PubMed](#)]
39. Jackson, A.J.; Tiana, D.; Walsh, A. A universal chemical potential for sulfur vapours. *Chem. Sci.* **2016**, *7*, 1082–1092. [[CrossRef](#)] [[PubMed](#)]
40. West, E.D. The heat capacity of sulfur from 25 to 450°, the heats and temperatures of transition and fusion. *J. Am. Chem. Soc.* **1959**, *81*, 29–37. [[CrossRef](#)]
41. Maruyama, S.; Aihara, T. Heat transfer from a layer of a carbon fiber cluster at low Reynolds numbers. *Exp. Therm. Fluid Sci.* **1994**, *8*, 128–134. [[CrossRef](#)]
42. Khaliji Oskouei, M.; Tamainot-Telto, Z. Investigation of the heat transfer properties of granular activated carbon with R723 for adsorption refrigeration and heat pump. *Therm. Sci. Eng. Prog.* **2019**, *12*, 1–12. [[CrossRef](#)]
43. Lee, D.-G.; Park, J.-H.; Lee, Y.-H.; Baeg, C.-Y.; Kim, H.-J. Natural convection heat transfer characteristics in a canister with horizontal installation of dual purpose cask for spent nuclear fuel. *Nucl. Eng. Technol.* **2013**, *45*, 969–978. [[CrossRef](#)]
44. Smith, R.L. Predicting evaporation rates and times for spills of chemical mixtures. *Ann. Occup. Hyg.* **2001**, *45*, 437–445. [[CrossRef](#)]
45. Guo, Z.; Roache, N.F. Overall mass transfer coefficient for pollutant emissions from small water pools under simulated indoor environmental conditions. *Ann. Occup. Hyg.* **2003**, *47*, 279–286.
46. Dalin, G.A.; West, J.B. The viscosity of sulfur vapor. *J. Phys. Chem.* **1950**, *54*, 1215–1221. [[CrossRef](#)] [[PubMed](#)]
47. West, W.A.; Menzies, A.W.C. The vapor pressures of sulfur between 100° and 550° with related thermal data. *J. Phys. Chem.* **1929**, *33*, 1880–1892. [[CrossRef](#)]
48. Lekakou, C.; Edwards, S.; Bell, G.; Amico, S.C. Computer modelling for the prediction of the in-plane permeability of non-crimp stitch bonded fabrics. *Compos. A Appl. Sci. Manuf.* **2006**, *37*, 820–825. [[CrossRef](#)]
49. Ozgumus, T.; Mobedi, M.; Ozkol, U. Determination of kozeny constant based on porosity and pore to throat size ratio in porous medium with rectangular rods. *Eng. Appl. Comput. Fluid Mech.* **2014**, *8*, 308–318. [[CrossRef](#)]
50. Rutt, M.; Lekakou, C.; Smith, P.A.; Sordon, A.; Santoni, C.; Meeks, G.; Hamerton, I. Methods for process-related resin selection and optimisation in high-pressure resin transfer moulding. *Mater. Sci. Technol.* **2018**, *35*, 327–335. [[CrossRef](#)]

51. Dutta, D.; Gope, S.; Negi, D.S.; Datta, R.; Sood, A.K.; Bhattacharyya, A.J. Pressure-induced capillary encapsulation protocol for ultrahigh loading of sulfur and selenium inside carbon nanotubes: Application as high performance cathode in Li–S/Se rechargeable batteries. *J. Phys. Chem. C* **2016**, *120*, 29011–29022. [[CrossRef](#)]
52. Lekakou, C.N.; Richardson, S.M. Simulation of reacting flow during filling in reaction injection moulding (RIM). *Polym. Eng. Sci.* **1986**, *26*, 1264–1275. [[CrossRef](#)]
53. Elsayed, Y.; Lekakou, C.; Tomlins, P. Modeling, simulations, and optimization of smooth muscle cell tissue engineering for the production of vascular grafts. *Biotechnol. Bioeng.* **2019**, *116*, 1509–1522. [[CrossRef](#)] [[PubMed](#)]
54. Liu, T.; Hu, H.; Ding, X.; Yuan, H.; Jin, C.; Nai, J.; Liu, Y.; Wang, Y.; Wan, Y.; Tao, X. 12 years roadmap of the sulfur cathode for lithium sulfur batteries (2009–2020). *Energy Storage Mater.* **2020**, *30*, 346–366. [[CrossRef](#)]